ORIGINAL RESEARCH ARTICLE

Hardness Prediction of the Heat-Affected Zone in Multilayer Welded SUS316 Stainless Steel Based on Dislocation Density Change Behavior

LINA YU, KAZUTOSHI NISHIMOTO, HIROYUKI HIRATA, and KAZUYOSHI SAIDA

The effects of strain hardening and recovery/recrystallization on the hardness of the heat-affected zone (HAZ) in multilayer welded austenitic stainless steel SUS316 were investigated in this study. The results revealed that strain hardening due to welding strain and softening due to recovery/recrystallization were the dominant factors affecting the hardness change in the HAZ during multilayer welding process. Furthermore, the relationship between the strain and dislocation density and that between the recovery/recrystallization and dislocation density were quantitatively investigated using positron annihilation lifetime spectroscopy. Based on these results, a new hardness prediction method based on the change in dislocation density in the HAZ during multilayer welding was proposed. The hardness values in the HAZ after the multilayer welding were predicted based on the simulated strain and thermal history, and the calculated hardness values agreed well with the measured results. This indicates that the newly proposed hardness prediction method based on the dislocation density change behavior in the HAZ during multilayer welding is valuable and effective for selecting the appropriate welding conditions before actual welding.

https://doi.org/10.1007/s11661-024-07318-7
© The Author(s) 2024

I. INTRODUCTION

STRESS corrosion cracking (SCC) in welded components of austenitic stainless steel is one of the significant aging degradation problems in nuclear power plants. SCC is caused by the superimposition of material, stress, and environmental factors.[1,2] For the material factor, low-carbon stainless steel was developed and applied as a countermeasure to prevent the formation of a chromium-deficient layer (sensitization) caused by chromium carbide precipitation.[3,4] However, in recent years, SCC has been confirmed to occur near the welds of low-carbon austenitic stainless steel pipes, even in areas where sensitization has not occurred.[5,6] Subsequent studies reported that when hardening occurred in the material, the SCC susceptibility[7,8] and SCC growth rate increased,[9] regardless of the presence or absence of sensitization. Because hardening has also been confirmed in welded components where SCC occurred, the hardening phenomenon due to welding has attracted attention.

Austenitic stainless steel has a strong tendency for strain hardening owing to its fcc crystal structure and low stacking fault energy. High plastic strain can accumulate during a multilayer welding process. On the other hand, the accumulated strain hardening can be reduced or even eliminated during the welding thermal cycle owing to recovery/recrystallization and grain growth. For austenitic stainless steels, the effects of strain hardening,[10] recovery/recrystallization,[11] dynamic strain aging,[12,13] and other phenomena related to the hardness change have been studied. However, hardening in the welded heat-affected zone (HAZ) has been studied primarily from a mechanical viewpoint, focusing only on stress and strain; few studies from a material viewpoint are available. Therefore, the hardening mechanism in a multilayer welded HAZ has not yet been clarified. To elucidate the hardening mechanism, the dominant factor affecting the hardness change in the HAZ is to be clarified first. Furthermore, hardness prediction in the multilayer welded HAZ based on the hardening mechanism before the actual welding is crucial for welding safety.

Therefore, herein, the effect of each phenomenon on the change in hardness was investigated by tensile and thermal aging tests on pre-strained materials simulating the HAZ in austenitic stainless steel JIS SUS316. The hardening mechanism in the multilayer welded HAZ

LINA YU, KAZUTOSHI NISHIMOTO, HIROYUKI HIRATA, and KAZUYOSHI SAIDA are with the Graduate School of Engineering, Osaka University, 2-1 Yamadaoka, Suita, Osaka 565-0871, Japan. Contact e-mail: yulina@mapse.eng.osaka-u.ac.jp; yulina@mapse.osaka-u.ac.jp
Manuscript submitted August 10, 2023; accepted January 2, 2024.
Article published online March 19, 2024

was also discussed from the material viewpoint. The essence of hardness is the ease of dislocation movements mainly due to changes in dislocation density. When multiple phenomena are considered at the same time, it is necessary to discuss the relationship between the phenomena with dislocation density. Therefore, the relationship between the dominant phenomena of hardness change and dislocation density was quantitatively investigated using the positron annihilation lifetime method.

Positron annihilation lifetime spectroscopy (PALS) is a non-destructive method that enables the nano-scale characterization of open-volume defects such as atomic vacancies and dislocations. Because positrons have a positive charge, they disappear at interstitial positions away from the positively charged nucleus if there are no voids or defects. When voids or defects exist in a material, they are trapped, and then pair-annihilate with the surrounding electrons. Hence, the lifetime of positrons is inversely proportional to the probability that electrons and positrons meet, that is, the product of the electron and positron densities. As the electron density at the defect position is lower than that at the interstitial position, the positron lifetime increases if voids or defects are present in the material. In addition, if the density of lattice defects is higher, the proportion of positrons trapped at the defect position is higher; thus, the positron lifetime increases.[14–17]

Based on the observed results, a new hardness prediction method based on the dislocation density change behavior in the HAZ during multilayer welding was proposed, and the validity of the prediction method was experimentally verified.

II. MATERIALS AND METHODS

In this study, austenitic stainless steel SUS316 was used as the base material, and YS316 was used as the welding wire; their chemical compositions are listed in Table I.

Tensile tests were performed at room temperature of 20 °C to investigate the strain hardening behavior of SUS316. The shape of the tensile test piece is illustrated in Figure 1, which is the sample shape required by the laser heating tensile equipment. The strain rate was set as 4.2×10^{-5} s^{-1} to investigate the relationship between strain and dislocation density, and the relationship between dislocation density and hardness.

A pre-strained material simulating the strain caused by welding was fabricated to study the recovery and recrystallization phenomena. To improve uniformity and prevent temperature rise during rolling, the plate material was cold-rolled by 20 pct using multipass rolling at low speed and low reduction rate. The test pieces were cut from the central part of the rolled sample, and the test was performed on the cross section parallel to the rolling direction. The specimens were cut using electrical discharge machining, which would cause the minimal damage to the original state of the material.

The specimens were subjected to various heat treatments to investigate the hardness and dislocation density reduction behaviors due to recovery and recrystallization. The simulated HAZ thermal cycles were applied to a 20 pct-rolled sample using a high-frequency induction heating apparatus. The heating rate was 100 °C/s, and the peak temperature was varied from 600 °C to 1300 °C with a holding time of 1 s and then cooled at a cooling rate of approximately 50 °C/s in an atmosphere of pure argon. Table II lists the heat treatment conditions used for the kinetic study of the dislocation density reduction behavior owing to recovery and recrystallization. The samples were thermally aged at 300 °C to 950 °C for various holding times with water cooling for all cases. For comparison, some specimens were also annealed at 1100 °C for 1 h and then quenched into water for solution treatment (ST).

Vickers hardness tests were conducted to study the changes in hardness owing to each phenomenon. After polishing, the Vickers hardness at the center of the tensile specimen was measured under a load of 0.098 N for 15 s, and the average value, excluding the maximum and minimum values, was obtained from multiple measurements.

Microstructural observations were performed using scanning electron microscopy (SEM) and electron back scattered diffraction (EBSD). Prior to SEM observation, the samples were polished and electrolytically etched using the 10 pct oxalic acid solution at room temperature. Prior to EBSD observation, the samples were electropolished with 15 pct perchloric acid ethanol at a voltage of 5.0 V, a current of 0.5 A, and a time of about 30 s.

PALS was used to characterize the lattice defects in the samples. Positron lifetime measurements were performed using a digital oscilloscope system with photomultiplier tubes mounted on BaF_2 scintillators. A Na-22 thin-film NA351 positron source was used as the positron beam source, and the positron lifetime was measured in an atmosphere at room temperature sandwiched between two samples, with approximately

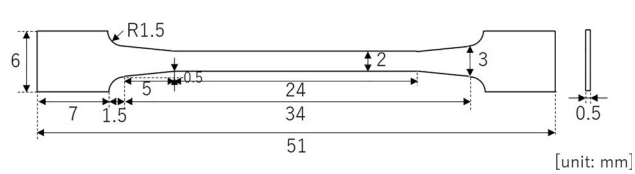

Fig. 1—Tensile specimen for tensile test.

Table I. Chemical Compositions of Materials (Mass Pct)

Material	C	Si	Mn	P	S	Ni	Cr	Mo	Co	Fe
SUS316	0.04	0.60	0.93	0.034	0.004	10.16	16.83	2.06	0.20	Bal.
YS316	≦ 0.08	≦ 0.65	1.0-2.5	≦ 0.03	≦ 0.03	11.0-14.0	18.0-20.0	2.0-3.0	—	Bal.

3×10^6 coincidence counts collected. In addition, the test pieces were electropolished with 15 pct perchloric acid ethanol to remove the oxide film formed on the surface.

Figure 2(a) shows a schematic of the lattice defect detection using PALS, and Figure 2(b) shows an example of PALS peak fit. Positron lifetime spectra were analyzed using the RESOLUTION[18] and POSITRONFIT Extended[19] programs. The dislocation density change behavior was quantitatively investigated through multicomponent analysis of the spectra obtained by using the following Eq. [1].

$$N(t) = \sum_{i=1}^{n} \frac{I_i}{\tau_i} \exp\left(-\frac{t}{\tau_i}\right) \qquad [1]$$

Here, N(t) is the counting rate, I is relative intensity, τ is positron lifetime, n is the component, and t is time.

Three-component analysis was used to evaluate the dislocation density, using the following Eq. [2].

$$C_d = \frac{1/\tau_f - 1/\tau_d + I_v(1/\tau_d - 1/\tau_v)}{1 - I_d - I_v} \times \frac{I_d}{\mu_d} \qquad [2]$$

Here, C is defect concentration, I is relative intensity, τ is positron lifetime, μ is trapping coefficient, f is free positron, d is dislocation, and v is vacancy. τ_f is the lifetime of free positrons, and the value is 102 ps. The trapping coefficient used in this study is shown as follows: $\mu_d = 5.1 \times 10^{-4}$ m^2s^{-1}.

Table II. Heat Treatment Conditions for Recovery or Recrystallization Analysis

Temperature (°C)	Holding Time (s)
300	3, 10, 30
400	1, 10, 30
500	1, 10, 30
600	1, 10, 30, 100
800	1, 30
850	150, 300, 600, 1000
900	30, 60, 120, 180
950	3, 7, 15, 30

A TIG multilayer welding test was performed on SUS316 using the wire of YS316, which has similar chemical compositions to that of the base metal. The shape of the specimen is shown in Figure 3, and the welding conditions are listed in Table III. A U-shaped groove with a groove angle of 20 deg, groove depth of 12 mm, and groove radius of 4 mm was applied to the center of the specimen, and multilayer welding was performed with 7 layer – 13 pass. After multilayer welding, hardness measurements were conducted on the cross section after polishing.

The thermal history and strain in the multilayer welds were simulated using FEM (Finite Element Method) simulation software JWRIAN, which was specifically developed for predicting the thermal history, residual stress, and deformation of welds.[20,21] Figure 4 shows the cross section of the 7-layer welds, with the dashed line indicating the bond boundary. Based on the actual cross section, the mesh model of 7-layer welds was created using the PATRAN software. Figure 5 shows the analysis model, dimensions, and boundary conditions. The element used for the analysis was a 4-node generalized plane strain element. Boundary conditions were three-point constrained to prevent rigid body deformation. A moving welding heat source was used in the welding analysis. The node distance in the WM and HAZ was set as 0.3 mm, which was much finer than that in the BM. The time integration was set as 0.2 s, which was small enough for dislocation density calculation. The melting point of SUS316 steel is 1400 °C, and the temperature-dependent material properties[22] are shown in Figure 6.

III. FACTORS AFFECTING THE HARDNESS CHANGE IN MULTILAYER WELDED HAZ

A. *Effect of Strain on Hardness Change*

The effect of weld-induced strain on the hardness change in the HAZ was investigated. After the tensile tests at room temperature with various strains, hardness measurements were performed on each specimen to investigate the relationship between plastic strain and hardness. Figure 7 shows the relationship between the equivalent plastic strain and Vickers hardness. The

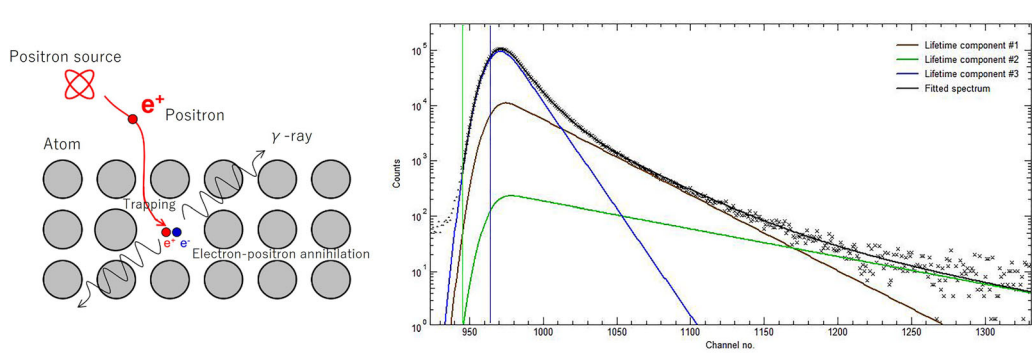

(a) a schematic of the lattice defect detection using PALS (b) an example of PALS peak fitv

Fig. 2—Schematic diagram of positron annihilation lifetime technique.

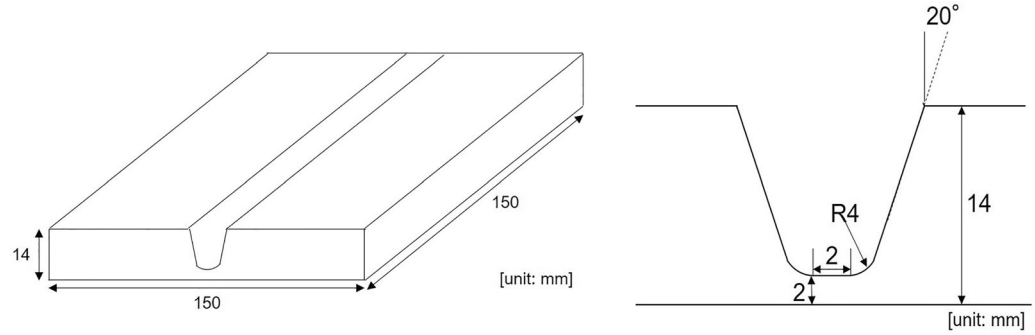

(a) Overall view (b) Groove shape

Fig. 3—Schematic diagram of specimen for multilayer welding.

Table III. Welding Conditions for Multilayer Welding

Layer	Pass	Current (A)	Voltage (V)	Wire Feed Rate (mm/s)	Welding Speed (mm/s)
1	1	250	15–16	45	1.67
2	2	220	14–15	45	1.67
3	3 ~ 4	220	14–15	45	1.67
4	5 ~ 6	220	14–15	45	1.67
5	7 ~ 8	220	14–15	45	1.67
6	9 ~ 10	220	14–15	45	1.67
7	11 ~ 13	220	14–15	45	1.67

Vickers hardness was the average value obtained from multiple measurements, and the error bars showed the difference between the maximum/minimum value and the average value. The equivalent plastic strain was calculated from the elongation and width of the parallel section and plate thickness before and after the tensile test using the following formula (3)[23]: Here, ε_{eq} is the equivalent plastic strain, dl/l, dw/w, and dt/t are the strain in the tensile, width, and thickness directions, respectively.

$$\varepsilon_{eq} = \sqrt{\frac{2}{3}}\sqrt{(dl/l)^2 + (dw/w)^2 + (dt/t)^2} \qquad [3]$$

The hardness significantly increased with increasing equivalent plastic strain. Although the welding strain in the multilayer welded HAZ differs depending on the welding conditions, welding shapes, and other factors, a maximum welding strain of ~ 20–25 pct can be introduced into the multilayer welded HAZ.[24,25] This suggests that the strain introduced in the multilayer welded HAZ can cause an increase in the hardness by ~ 100 HV, indicating that strain hardening by weld strain significantly affects the hardness change in the multilayer welded HAZ.

B. *Effect of Recovery/Recrystallization on Hardness Change*

To investigate the effect of recovery and recrystallization caused by the thermal cycle during welding on hardness change, the pre-strained 20 pct -rolled specimens simulating welding strain were heated at various peak temperatures with a holding time of 1 s to simulate the thermal cycles in HAZ. Vickers hardness measurements were performed after the thermal treatment, and the hardness results are shown in Figure 8. In the figure, the hardness values before thermal treatment (309 HV) and after solution treatment (200 HV) are indicated by dashed lines. The hardness decreased as the peak temperature increased and softened to the same level as the hardness of the base metal when the peak temperature was > 1050 °C, even after thermal treatment for 1 s. This result suggests that the work-hardened areas due to welding would be softened owing to recovery and recrystallization during the welding thermal cycle.

C. *Discussion of the Factors that Affected the Hardness Change in Multilayer Welded HAZ*

It has been reported that a maximum strain of ~ 20 to 25 pct can occur in multilayer welded HAZ, although this varies depending on the welding conditions, welding shapes, and so on.[24,25] From the results in Figure 7, it is possible that hardening of 100 HV or more would occur when a strain of 20 pct is introduced into HAZ, suggesting that strain hardening due to weld strain exerts a significant effect on the hardness change in the HAZ. In addition, recovery and recrystallization may also occur when strain hardening occurs owing to the welding thermal effects. In particular, the part near the melting point may be softened to the level of the base material owing to recrystallization, indicating that softening due to recovery/recrystallization also significantly affects the hardness change in the multilayer welded HAZ. Further, the authors have found that dynamic strain aging may affect the hardness in HAZ,

but the maximum hardening due to dynamic strain aging caused by a 30 pct strain was ~ 10 HV.[12] Compared to the strain hardening due to welding strain and softening due to recovery/recrystallization, the effect of dynamic strain aging on hardness was relatively small. This suggests that strain hardening due to the welding strain and softening due to recovery/recrystallization are the dominant phenomena affecting the hardness change in the HAZ during the multilayer welding process.

Strain hardening is caused by the multiplication of dislocations, which hinders their movement when applying strain. Softening due to recovery/recrystallization occurs because of the annihilation of lattice defects, such as dislocations. Therefore, the change in hardness in the HAZ is the change in dislocation density during the welding process. If the quantitative relationship between strain and dislocation density and quantitative dislocation density change during thermal cycles are known, the increment and annihilation of dislocation density can be predicted by simulating the strain behavior and thermal history in the HAZ using thermo-elastic-plastic analysis. Based on these results, the change in hardness in the HAZ of multilayer welded SUS316 stainless steel can be predicted from the change in dislocation density.

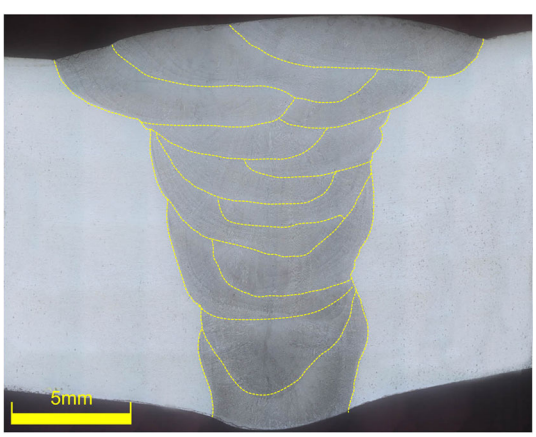

Fig. 4—Cross-sectional view of multilayer welds.

IV. DISLOCATION DENSITY INCREASE BEHAVIOR DUE TO STRAIN

To investigate the relationship between the equivalent plastic strain and the dislocation density of SUS316, tensile tests were performed at room temperature of 20 °C with strains varying from 5 to 30 pct. After the tensile tests, the dislocation densities of the specimens were measured using the positron lifetime method.

Figure 9 shows the relationship between the equivalent plastic strain applied by the room-temperature tensile test and dislocation density. As the equivalent plastic strain increased, the dislocation density increased monotonically. In addition, the relationship between strain and dislocation density obtained by positron lifetime spectroscopy in this study was approximately the same as that between the strain and dislocation density of SUS316L reported in previous studies.[26,27] The relationship between the equivalent plastic strain and dislocation density can be approximated by a straight line, and the relational expression is given by Eq. [4]. Here, ρ is the dislocation density (m^{-2}), and ε_{eq} is the equivalent plastic strain.

$$\rho = (6.53 \times \varepsilon_{eq} + 0.0024) \times 10^{15} \qquad [4]$$

Vickers hardness measurements were conducted on the specimens after the dislocation density measurement, and the relationship between the dislocation density and hardness is illustrated in Figure 10, which shows that the hardness increased with increasing the dislocation density.

Regarding the relationship between dislocation density and hardness, some previous studies have reported a linear relationship between the logarithm of dislocation density and hardness,[28] whereas other studies have reported a linear relationship between the square root of dislocation density and hardness.[29,30] Figure 11 shows the relationship between the hardness and dislocation density obtained in this study with the square root of the dislocation density. The relationship between the square root of the dislocation density and the hardness can be approximated by a straight line. As a result of deriving an approximation formula for the relationship between the dislocation density and hardness, the approximation formula is shown in Eq. [5]. Here, HV is the Vickers hardness, and ρ is the dislocation density (m^{-2}).

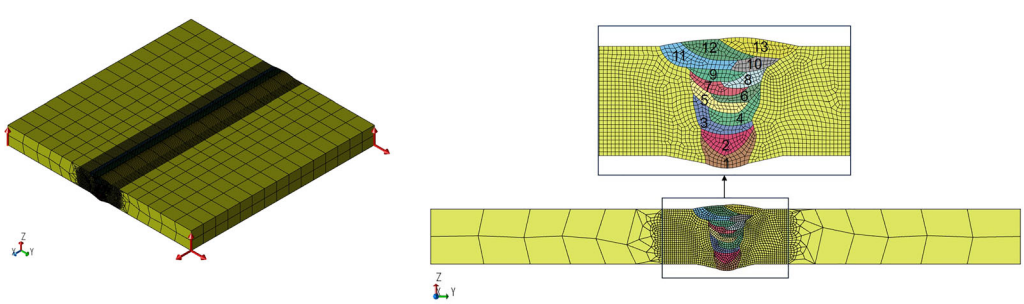

(a) Analysis model and boundary conditions

(b) Welding sequence

Fig. 5—FEM analysis model of multilayer welds.

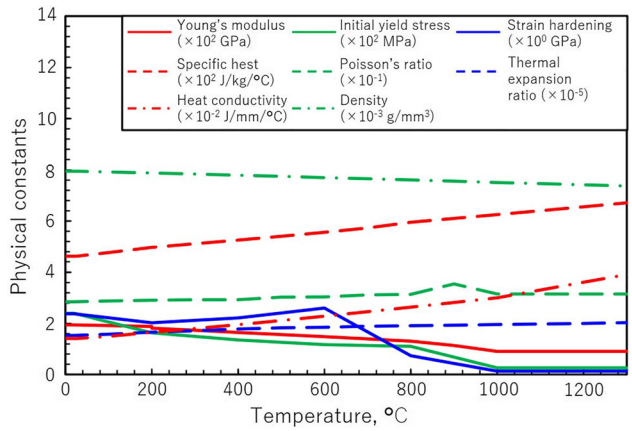

Fig. 6—Temperature-dependent material properties of SUS316 steel.

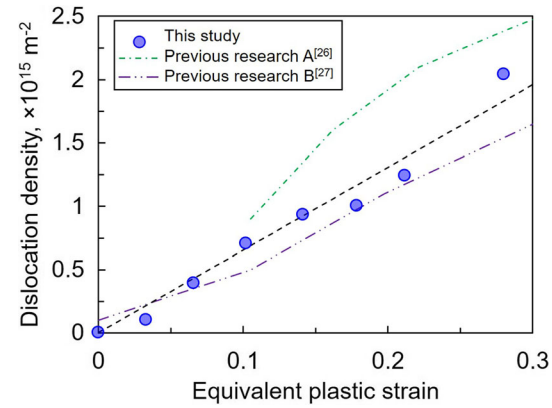

Fig. 9—Relationship between equivalent plastic strain and dislocation density.

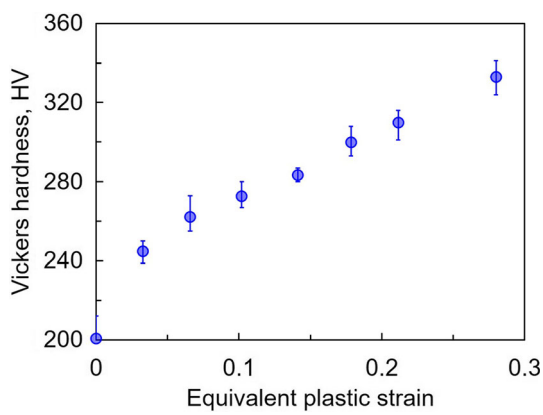

Fig. 7—Relationship between plastic strain and Vickers hardness at room temperature.

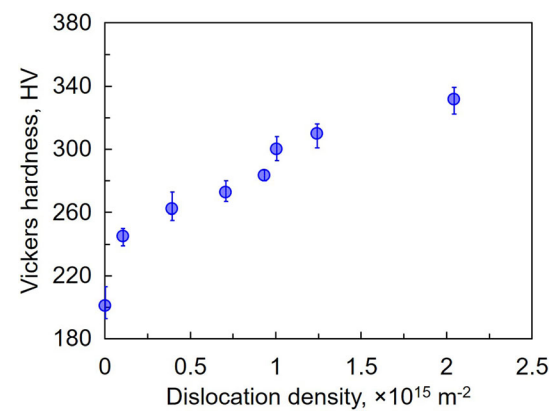

Fig. 10—Relationship between dislocation density and Vickers hardness.

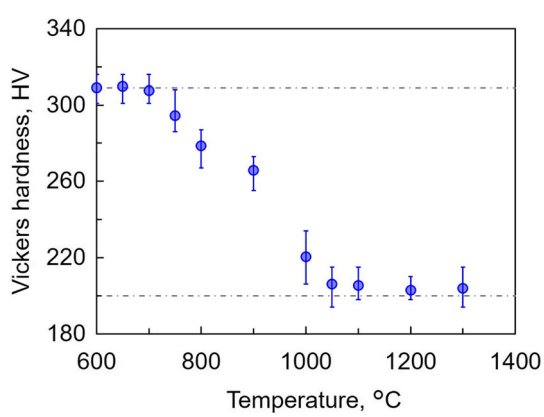

Fig. 8—Change of Vickers hardness due to heat treatment.

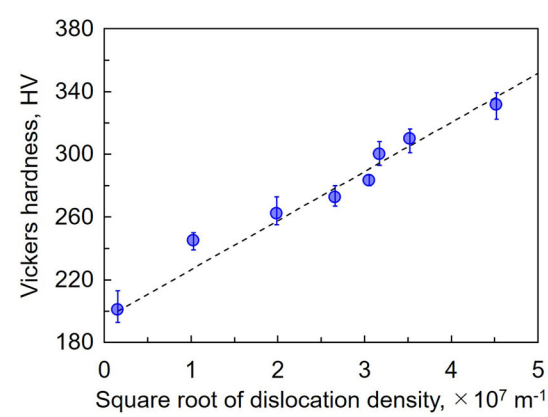

Fig. 11—Relationship between the square root of dislocation density and Vickers hardness.

$$HV = 3.13 \times 10^{-6} \times \left(\sqrt{\rho} - 1.23 \times 10^{6}\right) + 200 \quad [5]$$

Using the expressions obtained above, the increase in dislocation density during plastic deformation in SUS316 was quantitatively calculated, and the strain hardening behavior owing to the increase in dislocation density could also be predicted.

V. DISLOCATION DENSITY REDUCTION BEHAVIOR DUE TO RECOVERY/RECRYSTALLIZATION

A. *Dislocation Density Reduction Behavior After Thermal Aging*

To investigate the dislocation density reduction behavior during the thermal aging of SUS316, 20 pct -rolled material was thermally aged under the conditions

listed in Table II, and the dislocation density in the cross section parallel to the rolling direction was measured using positron annihilation lifetime spectroscopy. Figure 12 shows the dislocation density measured after thermal aging.

In the conditions with peak temperature < 600 °C, the dislocation density decreased monotonically with increasing thermal aging holding time, and after long-term aging, the dislocation density showed a constant value higher than that of the base metal. Figure 13 shows the microstructures of specimens aged at 600 °C, together with the specimen before thermal aging. Before and after thermal aging, no microstructural changes were observed, and several slip lines were observed even after thermal aging for 30 s. This suggested that the dislocation density change at temperatures < 600 °C is owing to the recovery phenomenon. In addition, the dislocation density after thermal aging at 600 °C for 100 s was approximately the same as that after 30 s, indicating that the dislocation density after full recovery was estimated to be ~ 7.2×10^{13} m^{-2}, which was sufficiently higher than that of the base metal (ST).

When aged at 800 °C, the dislocation density after thermal aging for 1 s was almost the same as that after thermal aging at 600 °C for 100 s. Little change in dislocation density was observed, which suggests that the recovery was completed immediately during the heating process or subsequent thermal aging at 800 °C for 1 s.

At thermal aging temperatures > 850 °C, the dislocation density decreased monotonically with increasing holding time and decreased to the same level as the base metal after long-term thermal aging. Figure 14 shows the microstructures observed in the specimens aged at 900 °C. The slip lines observed after cold rolling disappeared owing to the thermal aging, and some small recrystallized grains were observed. This suggested that the dislocation density decreased owing to the recrystallization phenomenon at temperatures > 850 °C.

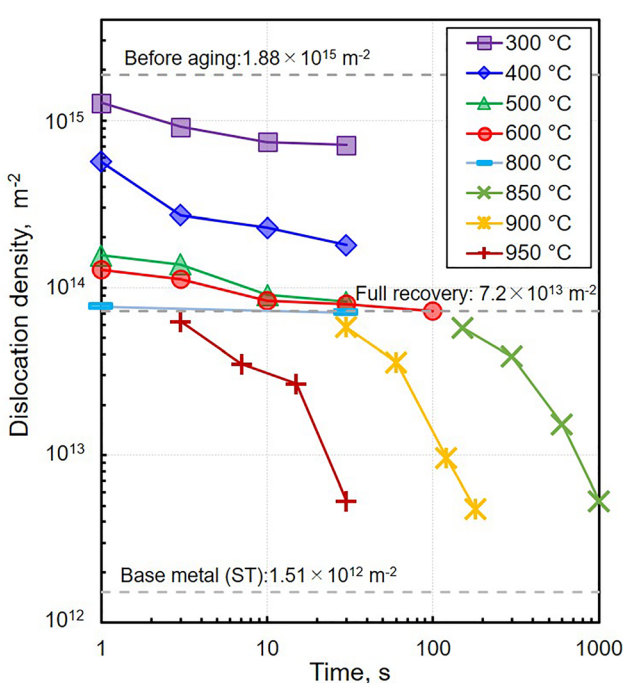

Fig. 12—Dislocation reduction behavior due to thermal aging.

B. *Kinetic Analysis of Dislocation Density Reduction Behavior Due to Recovery*

To understand the dislocation density reduction behavior due to the recovery phenomenon, the dislocation density reduction behavior during thermal aging at 300–600 °C was kinetically analyzed. In a previous study,[31] the hardness reduction behavior owing to recovery was kinetically analyzed, and when the recovery fraction was defined by Eq. [6], it was found that the hardness reduction behavior owing to recovery follows the Johnson–Mehl equation[32–34] (Eq. [7]). Here, HV_{before}: the hardness before aging, HV_{after}: the hardness after the completion of recovery, HV_{aged}: the hardness after thermal aging, f: the recovery fraction, K: the rate constant (s^{-1}), t: the time (s), and n: the exponent.

$$f = \frac{HV_{before} - HV_{aged}}{HV_{before} - HV_{after}} \quad [6]$$

$$f = 1 - \exp\{-(Kt)^n\} \quad [7]$$

Because a close correlation exists between the dislocation density and hardness, the recovery behavior can be similarly analyzed by defining the dislocation density reduction rate owing to recovery, as in Eq. [8]. Here, ρ_{before}: dislocation density before aging (m^{-2}), ρ_{after}: dislocation density after completion of recovery (m^{-2}), and ρ_{aged}: dislocation density after thermal aging (m^{-2}).

$$f = \frac{\rho_{before} - \rho_{aged}}{\rho_{before} - \rho_{after}} \quad [8]$$

In addition, by taking the logarithms of both sides of Eq. [7] and transforming it, it can be expressed as Eq. [9] below.

$$\ln\left\{\ln\left(\frac{1}{1-f}\right)\right\} = n\ln(t) + n\ln(K) \quad [9]$$

Figure 15 shows the Johnson–Mehl plots obtained using Eqs. [8] and [9] for the dislocation density reduction owing to the recovery phenomenon. The dislocation density after the completion of the recovery in Eq. [8] is 7.2×10^{13} m^{-2} obtained after the thermal aging at 600 °C for 100 s. The plot can be approximated as a straight line at any temperature, and the slope is approximately the same regardless of the temperature. This suggests that the reduction in dislocation density by recovery follows the Johnson–Mehl equation. The time exponent n (average slope) of the Johnson–Mehl plot was 0.2010.

In general, the rate constant K obtained from the Johnson–Mehl plot can be expressed using Eq. [11] by taking the logarithms of both sides of Eq. [10]. Here, K_0:

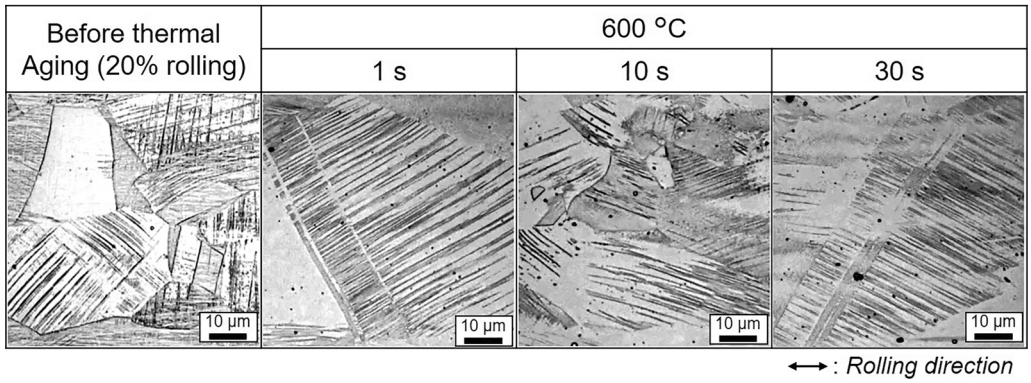

Fig. 13—Microstructures before and after thermal aging at 600 °C for 20 pct cold-rolled material.

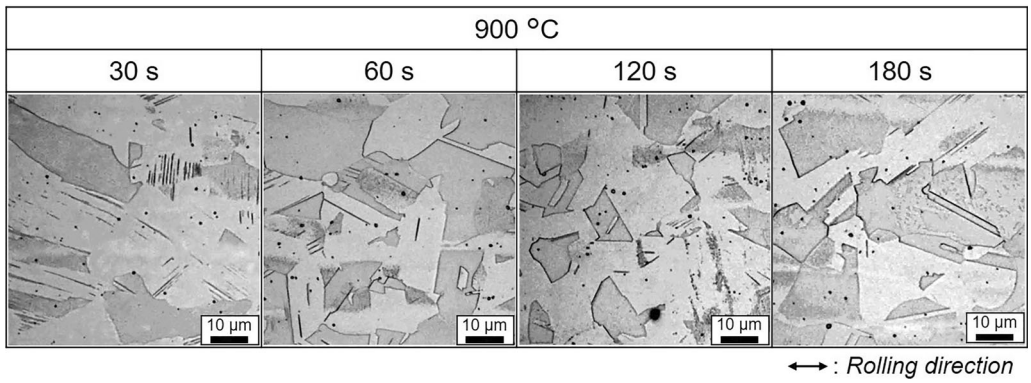

Fig. 14—Microstructures after thermal aging at 900 °C for 20 pct cold-rolled material.

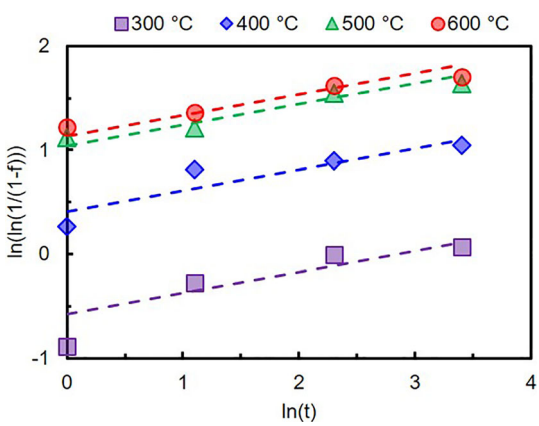

Fig. 15—Johnson–Mehl plot of dislocation reduction behavior due to recovery.

the rate constant (s^{-1}), Q: the activation energy, R: the gas constant (8.314 J/mol K), and T: the temperature (K).

$$K = K_0 \exp\left(-\frac{Q}{RT}\right) \quad [10]$$

$$\ln(K) = \ln(K_0) - \frac{Q}{RT} \quad [11]$$

Figure 16 shows the Arrhenius plot using Eq. [11] for K at each temperature, as obtained from the Johnson–Mehl plot shown in Figure 15. The results of the Arrhenius plot are approximated by a straight line. From the aforementioned results, it can be obtained that the activation energy for dislocation density reduction behavior owing to recovery is 122.9 kJ/mol, and the rate constant is 1.53×10^{10} s^{-1}.

C. *Kinetic Analysis of Dislocation Density Reduction Behavior Owing to Recrystallization*

Similar to recovery, the dislocation density reduction behavior owing to recrystallization was kinetically analyzed. The hardness reduction behavior owing to recrystallization followed the Johnson–Mehl equation; the rate constant followed the Arrhenius equation.[35] Therefore, the dislocation density reduction behavior owing to recrystallization can be kinetically analyzed by defining the dislocation density reduction rate owing to recrystallization similarly as in Eq. [8].

Figure 17 shows the Johnson–Mehl plots of the dislocation density reduction behavior owing to recrystallization after the thermal aging at 850–950 °C. The dislocation density before thermal aging was 7.2×10^{13} m^{-2}, and that after full recrystallization was 2.4×10^{12} m^{-2}, which was the same order of magnitude as that in the base metal (ST). The plot can be approximated as a straight line at any temperature,

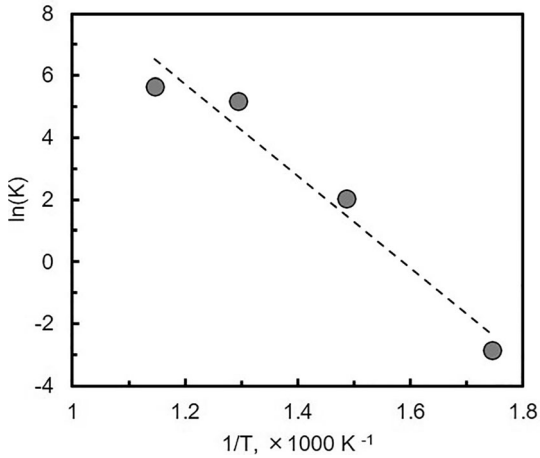

Fig. 16—Arrhenius plot of dislocation reduction behavior due to recovery.

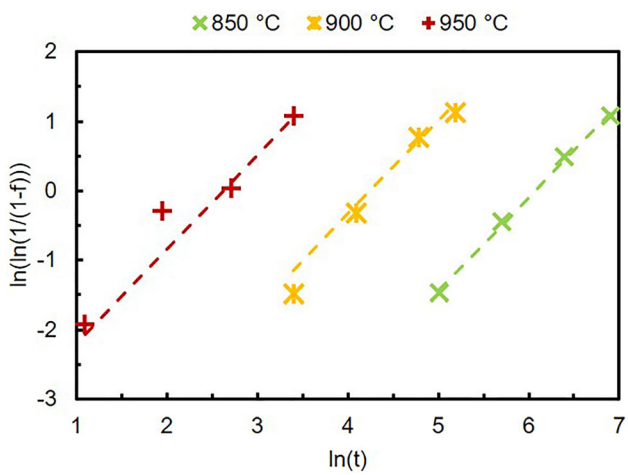

Fig. 17—Johnson–Mehl plot of dislocation reduction behavior due to recrystallization.

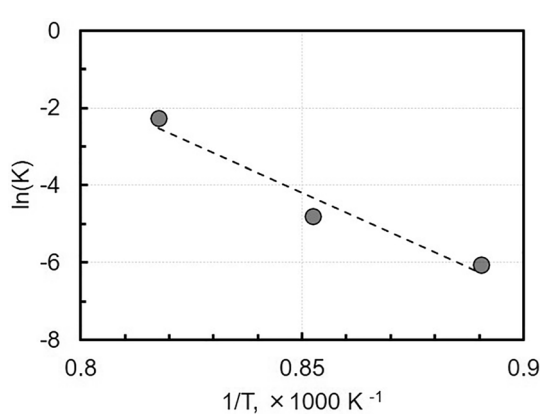

Fig. 18—Arrhenius plot of dislocation reduction behavior due to recrystallization.

and the slope is approximately the same regardless of the temperature. This suggests that the dislocation density reduction owing to recrystallization follows the Johnson–Mehl equation. The time exponent n (average slope) of the Johnson–Mehl plot was 1.3539.

Table IV. Comparison of Kinetic Constants of Dislocation Reduction Behavior Due to Recovery or Recrystallization

Constants	Recovery	Recrystallization
n	0.2010	1.3539
Q, kJ/mol	122.9	393.5
K_0, s^{-1}	1.53×10^{10}	4.68×10^{15}

Figure 18 shows the Arrhenius plot for K at each temperature obtained from the Johnson–Mehl plot. The Arrhenius plot can be approximated as a straight line, similar to the recovery. From the aforementioned results, it can be obtained that the activation energy of dislocation density reduction owing to recrystallization is 393.9 kJ/mol, and the rate constant is 4.68×10^{15} s^{-1}.

D. *Comparison of Kinetic Analysis of Recovery and Recrystallization*

The measurement results for the 20 pct -rolled material suggested that the dislocation density decreased owing to the recovery phenomenon at low temperatures and recrystallization at high temperatures. Table IV summarizes the constant values of n, Q, and K_0 obtained from the recovery and recrystallization kinetic analyses. The activation energy for recovery is much lower than that for recrystallization. The activation energy varied depending on the rate-determining mechanism of the phenomenon. This suggests that the rate-determining mechanisms for the dislocation density reduction behavior owing to recovery and recrystallization are different.

Table V lists the activation energies of self-diffusion and grain boundary diffusion for Fe, Cr, Ni, and Mo, which are the primary constituent elements of SUS316, in SUS316 or other austenitic stainless steels.[36–38] The activation energy for recovery obtained from the kinetic analysis was lower than that for lattice diffusion and was close to the activation energy for grain boundary diffusion of Fe and Cr. The previous study reported that the activation energy for recovery is ~ 0.47–0.7 for lattice diffusion,[38] and the activation energy for recovery obtained in this study is consistent with this trend. Moreover, the activation energy of recrystallization is the same order of magnitude as that of lattice diffusion.[38] The activation energy of recrystallization obtained from the kinetic analysis was close to or slightly larger than that of lattice diffusion, suggesting that the dislocation density reduction behavior owing to recrystallization is determined by lattice diffusion.

Even if the dislocation density decreases during thermal aging, recovery and recrystallization have different rate-determining mechanisms, suggesting that they should be considered separately.

E. *Cutoff Temperature for Recovery and Recrystallization*

Although dislocation density reduction behavior owing to recovery and recrystallization occurs during the thermal aging process, the mechanisms are different, suggesting that each phenomenon should be discussed separately. Therefore, the cutoff temperature for recovery and recrystallization was investigated.

The results of the dislocation density measurements for the 20 pct -rolled material revealed that the dislocation density decreased owing to recovery at a relatively low temperature for a short time and recrystallization at a high temperature for a long time. Under the condition at 800 °C even only for 1 s, the dislocation density decreased to the same level as that after full recovery, and approximately no change in dislocation density occurred after aging for 30 s. This implies that after short-term thermal aging at 800 °C, the recovery was completed instantaneously, and no reduction in dislocation density due to recrystallization occurred. In addition, it is inferred that the dislocation density decreased owing to recrystallization for long-term thermal aging at 800 °C. However, in a relatively short-term heat-affected process such as welding, the cutoff temperature of recovery/recrystallization is defined as the temperature at which recovery finishes instantaneously when the kinetic analysis of recovery is extrapolated to the high temperature side.

To investigate the boundary condition for recovery and recrystallization, the recovery fraction was calculated using Eq. [12], which is a combination of Eqs. [7] and [10].

$$f = 1 - \exp\left[-\left\{K_0 \exp\left(-\frac{Q}{RT}\right) \times t\right\}^n\right] \qquad [12]$$

Figure 19 shows the calculated recovery fraction after thermal aging for 1 s at various temperatures. At temperatures above ~ 800 °C, the recovery fraction after thermal aging for 1 s was > 99.9 pct, indicating that the recovery was nearly completed. This suggests that in a very short aging process such as welding, a temperature of ~ 800 °C is the cutoff temperature of recovery/recrystallization.

To confirm the result, the microstructures of 20 pct -rolled material before and after thermal aging at difference temperatures for 1 s were observed by EBSD. The microstructure of as cold-rolled material before the thermal aging is shown in Figure 20(a), in which the slip lines were observed and grain size was approximately 30 μm. Compared to the microstructure before thermal aging in Figure 20(a), no obvious microstructural change was observed at low temperature of 500 °C for 1 s, as presented in Figure 20(b). However, after thermal aging at 800 °C for 1 s, as illustrated in Figure 20(c), nearly no slip lines were observed and no small new grains appeared, indicating that the recovery was completed and the recrystallization did not occur. In addition, after thermal aging at 900 °C for 1 s, as shown in Figure 20(d), several small grains were observed and the grain size was much smaller than that at temperatures below ~ 800 °C, indicating that recrystallization has occurred. The above results suggest that for a very short-term aging process such as welding, a temperature of ~ 800 °C can be used as the cutoff temperature of recovery/recrystallization.

VI. HARDNESS PREDICTION METHOD BASED ON DISLOCATION DENSITY CHANGE BEHAVIOR IN MULTILAYER WELDED HAZ

A. *Construction of Hardness Prediction Method Based on the Prediction of Dislocation Density Change in Multilayer Welded HAZ*

The results in Section III suggest that the dominant factors for HAZ hardening during multilayer welding

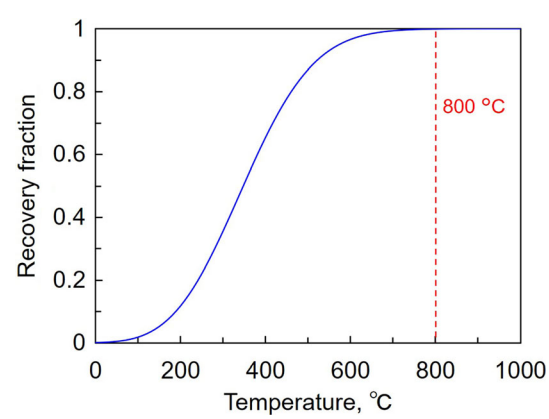

Fig. 19—Relationship between aging temperature and recovery fraction during 1 s thermal aging.

Table V. Activation Energy of Fe, Cr, Ni Diffusion in SUS316 or γ-Fe

Element	Material	Behavior	Activation Energy Q (kJ/mol)	Case
Fe	SUS316	lattice diffusion	229	A[36]
	SUS316	grain boundary diffusion	177	
Cr	SUS316	lattice diffusion	243	B[37]
	SUS316	grain boundary diffusion	191	
Fe	γ-Fe	lattice diffusion	270	C[38]
Cr	γ-Fe	lattice diffusion	170-406	
Ni	γ-Fe	lattice diffusion	283	
Mo	γ-Fe	lattice diffusion	247	

are strain hardening and softening owing to recovery/recrystallization. In addition, the relationship between strain and dislocation density increase behavior, and the relationship between recovery/recrystallization and dislocation density reduction behavior are quantitatively investigated in Sections IV and V, respectively. Subsequently, the dislocation density change behavior due to each phenomenon is clarified. However, in the HAZ, the increase in dislocation density owing to strain and reduction in dislocation density due to recovery/recrystallization co-occur at the same time. Therefore, to quantitatively predict the dislocation density change behavior in the HAZ, a new theoretical model was proposed in this study for simultaneously calculating the dislocation density increase behavior due to strain and dislocation density reduction behavior due to recovery/recrystallization.

First, based on the relationship between the strain and dislocation density given by Eq. [4] in Section IV, the increase in dislocation density in the HAZ can be calculated by the equivalent plastic strain obtained by a FEM simulation.

Second, the prediction method for the dislocation density reduction due to recovery/recrystallization was considered as follows: The reduction in the dislocation density due to recovery and recrystallization follows the Johnson–Mehl equation. Therefore, Eq. [14] can be obtained when the recovery/recrystallization fraction is defined by Eq. [13]. Here, ρ_{before}: dislocation density before thermal aging (m^{-2}), ρ_{after}: dislocation density after completion of recovery/recrystallization (m^{-2}), ρ_{aged}: dislocation density after thermal aging (m^{-2}), and f: recovery/recrystallization fraction. In addition, the rate constant K in the Johnson–Mehl equation follows the Arrhenius equation. It should be mentioned that only one dislocation reduction mechanism (recovery or recrystallization) is input into the algorithm for a given temperature and a given time step at a location on the simulation grid node.

$$f = \frac{\rho_{\text{before}} - \rho_{\text{aged}}}{\rho_{\text{before}} - \rho_{\text{after}}} \quad [13]$$

$$f = 1 - \exp\{-(Kt)^n\} \quad [14]$$

The addition rule was used to consider recovery and recrystallization in non-isothermal processes. A schematic of the addition rule is shown in Figure 21. The thermal cycle process can be divided into small-time intervals, and each can be treated as an isothermal process of minute duration.

Assuming a specific temperature, the thermal cycle parameter Kt can be derived from Eq. [15], which is an integral form of the Arrhenius equation for a small-time interval. Then, Eq. [14] can be used to calculate the dislocation density reduction behavior owing to recovery and recrystallization.

$$Kt = K_0 \sum_{i=1}^{n} (t_i - t_{i-1}) \times \exp\left(-\frac{Q}{RT_i}\right) \quad [15]$$

Finally, a method was proposed for the coupled prediction of dislocation density changes owing to strain and recovery/recrystallization. During the welding process, the strain increases because of the solidification shrinkage of the weld metal, and the dislocation density increases. As the dislocation density before thermal aging (ρ_{before}) changes with time, the recovery/recrystallization fraction f also changes. A new model for recovery/recrystallization considering the change in ρ_{before} was proposed for the coupled prediction of the

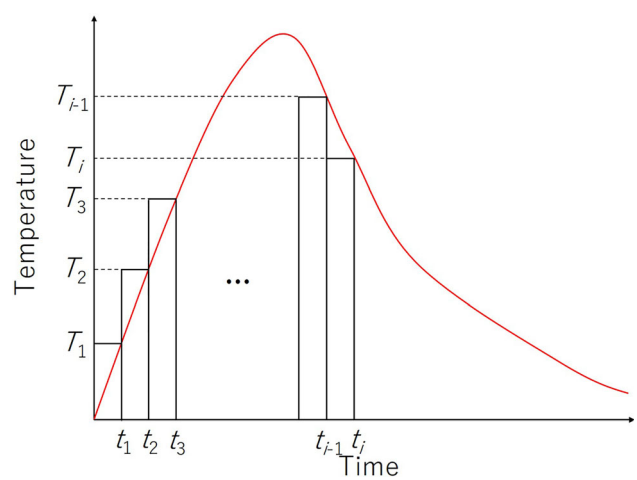

Fig. 21—Schematic of the additivity rule.

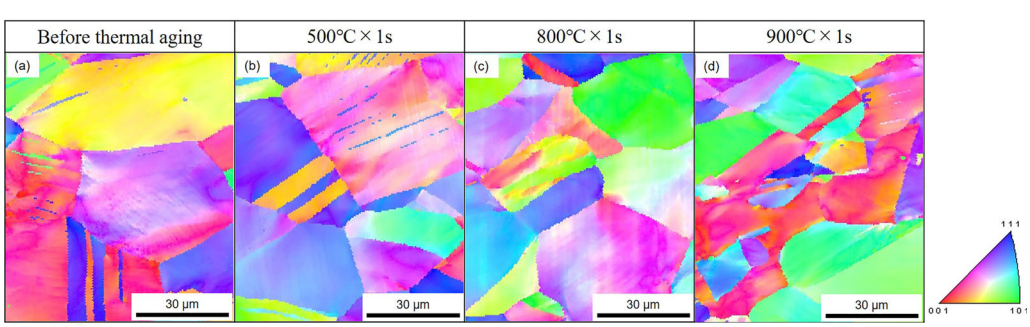

Fig. 20—Microstructure changes of 20 pct -rolled material before and after thermal aging at difference temperatures for 1 s.

dislocation density change behavior owing to strain and recovery/recrystallization during the welding process. Figure 22 shows a flowchart of the dislocation density change calculation owing to strain and recovery/recrystallization.

Figure 23 illustrates an example of simulated thermal history and weld strain history at a grid node in the HAZ of multilayer welding. Based on the simulated thermal history and weld strain history at each grid node, the dislocation density was calculated by the following method.

First, from the strain at time t_i obtained by thermal-elastic-plastic simulation, the dislocation density ρ_i without considering recovery and recrystallization is calculated using Eq. [4]. As shown in Eq. [16], the reduction of dislocation density $\Delta\rho_{i-1}$ owing to recovery/recrystallization at time t_{i-1} is subtracted from ρ_i, and the dislocation density ρ_i' before calculating the dislocation density decrease owing to recovery/recrystallization during $(t_{i-1} - t_i)$ can be calculated. Here, ρ_{i-1}'' is the dislocation density after recovery/recrystallization at time t_{i-1}. Using this ρ_i', the recovery/recrystallization fraction f_i' before calculating the dislocation density decrease owing to recovery/recrystallization during $(t_{i-1}–t_i)$ can be calculated by Eq. [17]. Here, ρ_{after} is the dislocation density after full recovery corresponding to ρ_i in the case of recovery and dislocation density of the base metal (2.4×10^{12} m^{-2}) in the case of recrystallization. Then, the thermal cycle parameter Kt_i' is obtained by Eq. [18]. Next, the thermal cycle parameter between t_{i-1} and t_i is calculated using Eq. [19] by addition rule. Finally, the recovery/recrystallization fraction, f_i'', was calculated using Eq. [20], and the dislocation density after recovery/recrystallization ρ_i'' can be obtained by Eq. [21].

$$\rho_i' = \rho_i - \Delta\rho_{i-1} = \rho_i - \left(\rho_{i-1} - \rho_{i-1}''\right) \quad [16]$$

$$f_i' = \frac{\rho_i - \rho_i'}{\rho_i - \rho_{after}} \quad [17]$$

$$Kt_i' = \left\{\ln\left(\frac{1}{1 - f_i'}\right)\right\}^{1/n} \quad [18]$$

$$Kt_i' = (t_i - t_{i-1}) \times K_0 \exp\left(-\frac{Q}{RT_i}\right) + Kt_i'' \quad [19]$$

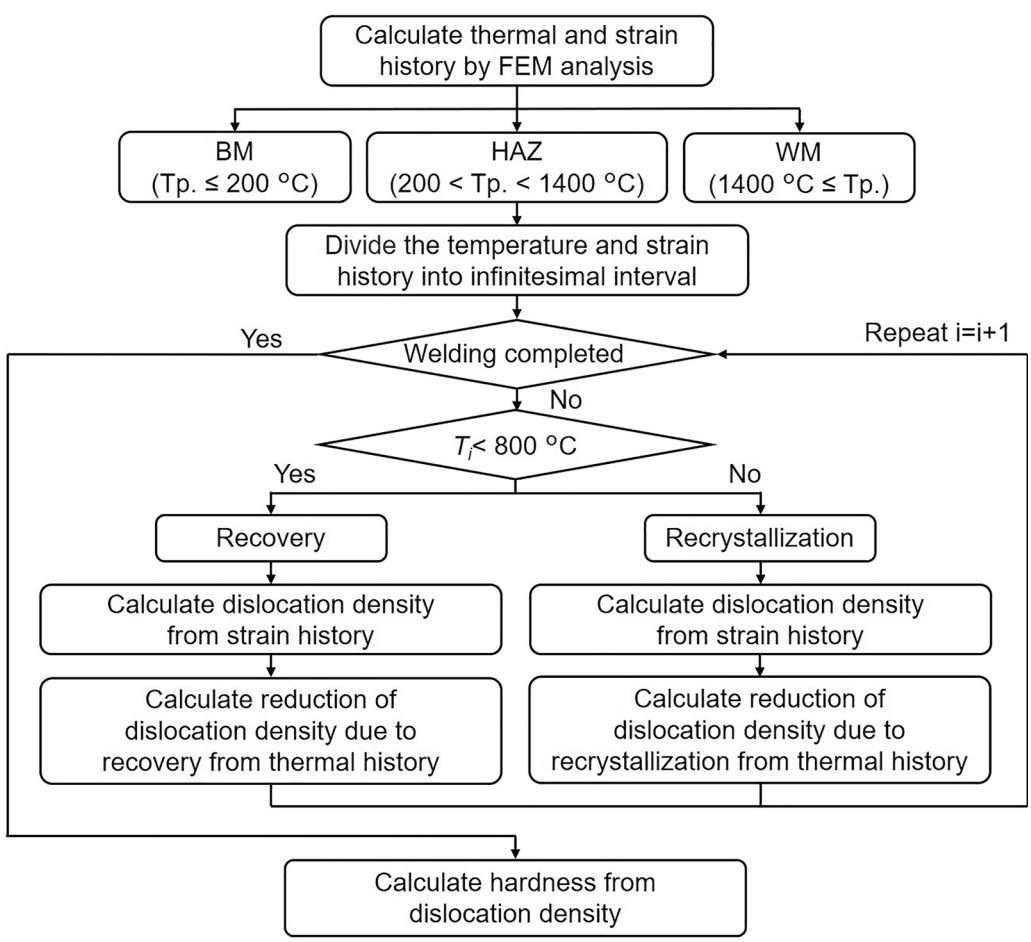

Fig. 22—Flowchart of hardness prediction in multilayer welded HAZ.

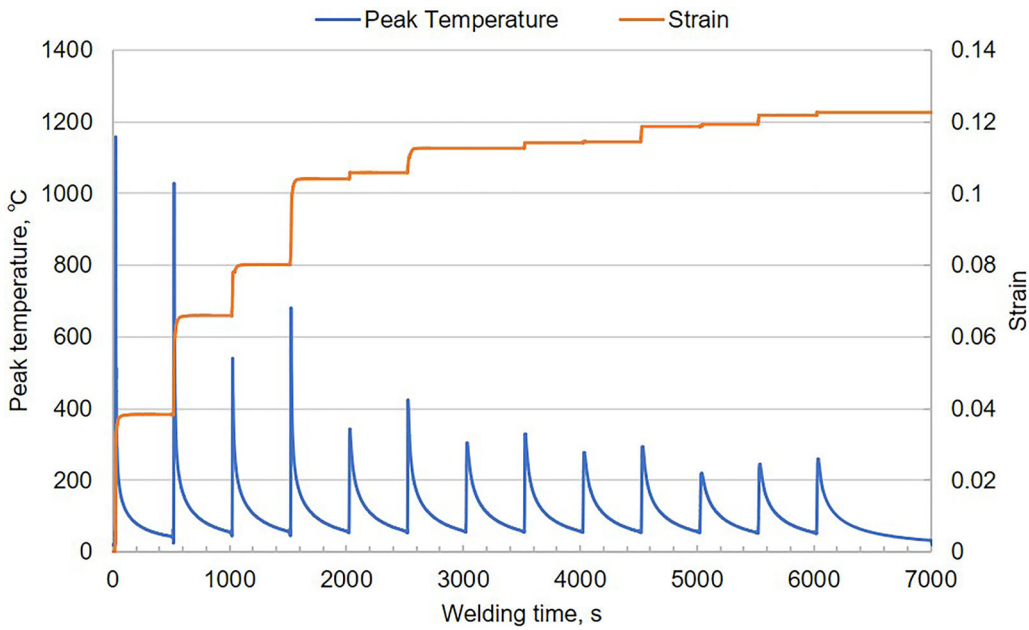

Fig. 23—An example of simulated thermal history and weld strain history at a grid node in the HAZ of multilayer welding.

$$f_i'' = 1 - \exp\{-(Kt_i'')^n\} \quad [20]$$

$$\rho_i'' = \rho_i - f_i'' \times (\rho_i - \rho_{\text{after}}) \quad [21]$$

The aforementioned calculations were performed for the entire welding process, and the final dislocation density was converted into hardness using Eq. [5] to predict the hardness change in the HAZ due to strain hardening and recovery/recrystallization.

The values of n, Q, and K_0 listed in Table IV were used to calculate recovery and recrystallization. In the calculation, points with peak temperatures > 1400 °C were treated as weld metal. The cutoff temperature for recovery and recrystallization was assumed to be 800 °C from the results shown in Figures 19 and 20 in Section V–E, and it was assumed that there would be no thermal effect at temperatures < 200 °C.

B. *FEM Simulation Results*

In this study, 7 layer − 13 pass welded sample was used to verify the effectiveness of the proposed hardness prediction system for multilayer welds. The thermal cycles in the multilayer welds were simulated using the thermal elastic-plastic FEM software JWRIAN, which was specifically developed for predicting the thermal history, residual stress, and deformation of welds.[20,21]

Figure 24 shows the simulated peak temperature distribution in the middle cross section after 7-layer welding. The simulated weld metal part is illustrated in red color with a peak temperature > 1400 °C. The deformation of welds was also considered in the simulation,[20,21] and the simulated shape of the weld metal matches that of the actual weld metal well, indicating that the FEM simulation results are appropriate. Figure 25 shows the simulated equivalent plastic strain distribution in the cross section after 7-layer welding. The strain was high near the fusion boundary and under-surface.

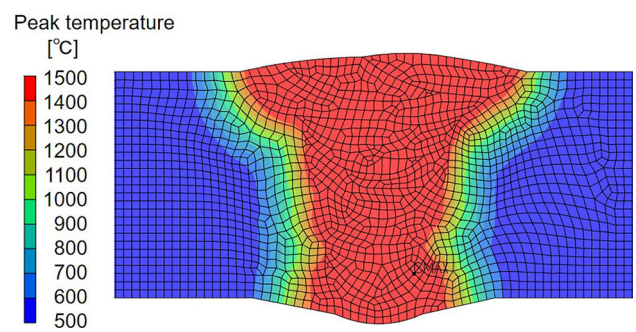

Fig. 24—Simulated peak temperature distribution after 7 layer − 13 pass welding.

C. *Hardness Predicted Result and Validity of the Proposed Hardness Prediction Method*

Based on the simulated thermal history and equivalent plastic strain history of each grid node, the hardness values in the HAZ were calculated using the proposed method. Because the temperature distribution shown in Figure 24 was generally symmetrical, the hardness distribution was observed only on the right side of the welding cross section. Figure 26(a) presents the predicted hardness distribution in the HAZ as a color chart map, with the hardness values displayed in rainbow colors for different hardness levels calculated using the method proposed in this study. For comparison, the predicted result calculated using only the equivalent plastic strain without considering recovery

and recrystallization is also shown in Figure 26(b). The hardness predicted by the proposed method in Figure 26(a) is lower than that calculated using only the equivalent plastic strain in Figure 26(b). Although hardening in the HAZ occurred with increased weld strain, softening owing to recovery and recrystallization occurred simultaneously, resulting in a considerably lower hardness value.

The hardness was experimentally measured in an actual welded cross section to verify the validity of the proposed hardness prediction method for multilayer welds. Figure 27 shows the two-dimensional mapping of the hardness values in the actual welded HAZ and the predicted results calculated using the proposed method. The hardness measurement was performed at intervals of 0.3 mm starting from the fusion boundary on the right side of the actual weld cross section. As shown in Figure 27(a), hardening is observed near the fusion boundary and under-surface, and no change in the hardness of the base metal was observed further away. Near the final layer weld, there were areas near the fusion boundary where the hardness was almost the same as that of the base material, and hardening was observed slightly away from the fusion boundary. As shown in Figure 27(b), the predicted hardness distribution agreed well with the experimentally measured results, both in terms of the hardness value and overall tendency.

In addition, as illustrated in Figure 28, a one-dimensional hardness comparison was performed between the measured and predicted values. Three measurement lines were set at z = 0, 7, and 14 mm, as shown in Figure 28(a). For comparison, the predicted hardness results considering only the strain without recovery/recrystallization were also included in the one-dimensional comparison. As shown in Figures 28(b)–(d), the hardness values predicted using the method proposed in this study, considering both strain and recovery/recrystallization, corresponded well with the measured values. However, the predicted hardness values considering only strain were significantly higher than the measured values.

These results indicate that the proposed hardness prediction method based on the dislocation density change behavior, which considers both strain and recovery/recrystallization, is valuable and effective. Therefore, appropriate welding conditions can be selected before actual multilayer welding, which is useful for multilayer welding in industry.

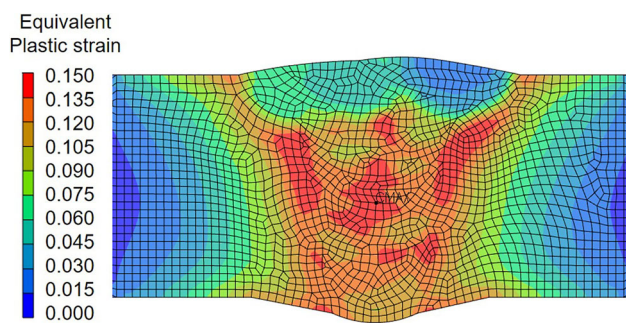

Fig. 25—Simulated equivalent plastic strain distribution after 7 layer – 13 pass welding.

VII. CONCLUSIONS

In this study, the effects of strain hardening and recovery/recrystallization on the hardness of a multilayer welded HAZ in austenitic stainless steel SUS316 were investigated, and the relationship between the phenomena and dislocation density change behavior was quantitatively analyzed using PALS. Based on these results, a new hardness prediction method based on dislocation density change behavior in the HAZ during multilayer welding was proposed. The following conclusions were drawn:

(1) The hardness results suggested that strain hardening due to welding strain and softening due to recovery/recrystallization were the dominant

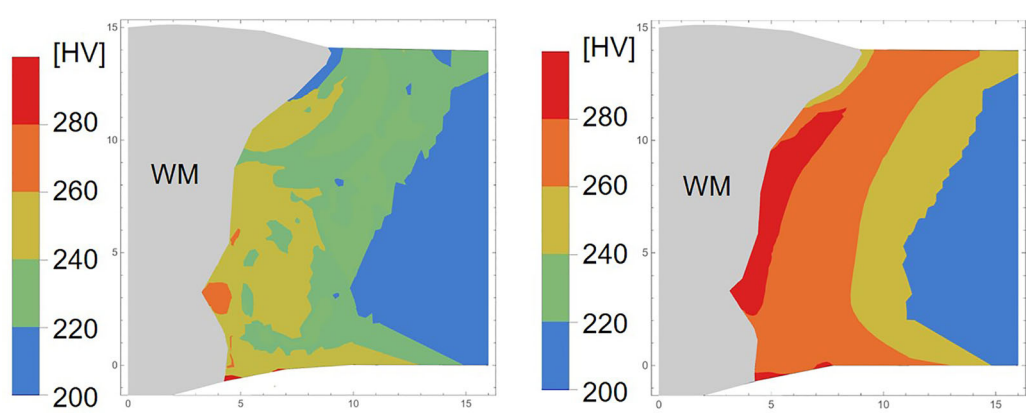

(a) Predicted hardness distribution by proposed method

(b) Predicted hardness distribution considered only strain

Fig. 26—Comparison of the predicted hardness distributions after multilayer welding calculated by two methods.

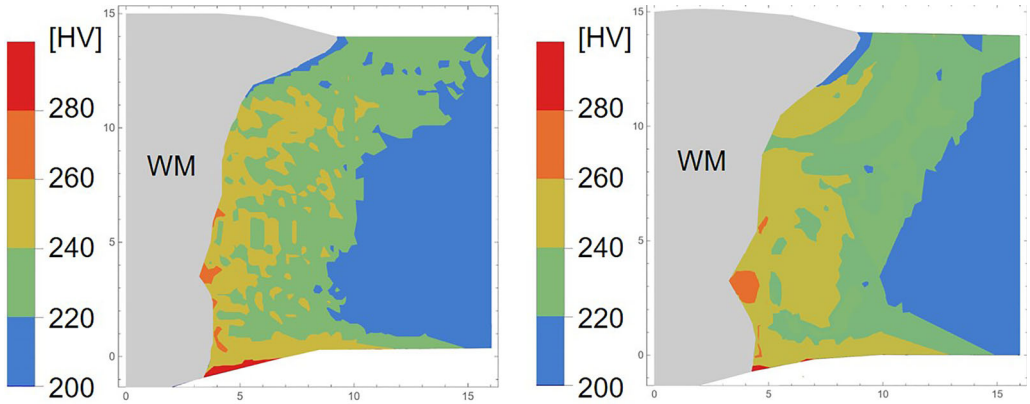

(a) Measured hardness distribution

(b) Predicted hardness distribution by proposed method

Fig. 27—Comparison of measured and predicted hardness distributions after multilayer welding.

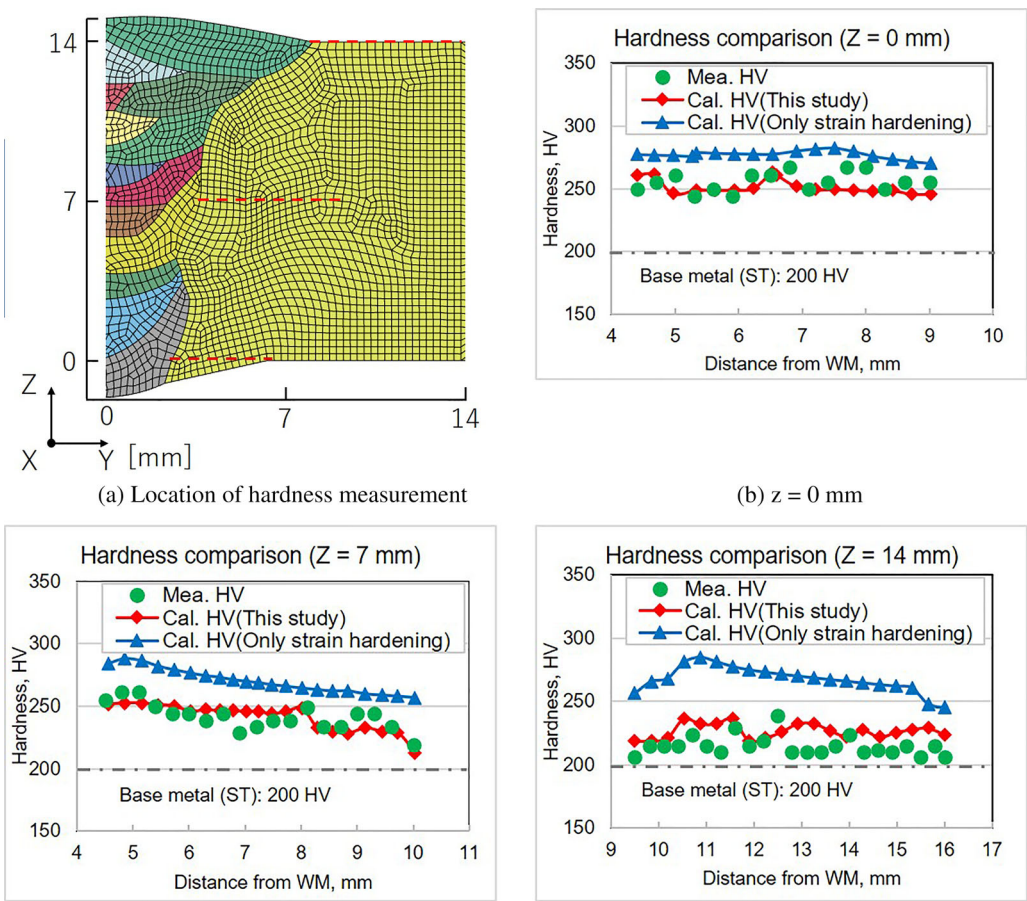

(a) Location of hardness measurement

(b) z = 0 mm

(c) z = 7 mm

(d) z = 14 mm

Fig. 28—Comparison of predicted and measured hardness distributions at the three lines after multilayer welding.

phenomena affecting the hardness change in the HAZ during the multilayer welding process.

(2) The increase in dislocation density due to strain was analyzed by PALS. The relationship between the square root of the dislocation density and hardness was approximated by a straight line, and a relational expression between the dislocation density and hardness was obtained.

(3) The decrease in dislocation density due to recovery at low temperatures and recrystallization at high temperatures was kinetically studied using the Johnson–Mehl equation and Arrhenius equation.

(4) A new hardness prediction method was proposed based on the coupled prediction of the increase in dislocation density due to strain and the decrease in dislocation density due to recovery/recrystallization.
(5) The predicted hardness results correspond well with the measured results, indicating that the proposed hardness prediction method is valuable and effective for selecting appropriate welding conditions before actual welding.

ACKNOWLEDGMENTS

This work was supported by Kansai Electric Power Co., Inc., Japan. The authors gratefully acknowledge the assistance of Professor Ninshu Ma of Osaka University with the FEM simulation. The authors gratefully acknowledge the assistance of Mr. Ikumi Asai, who holds a Master's degree from the Graduate School of Engineering, Osaka University, Japan.

FUNDING

Open Access funding provided by Osaka University.

CONFLICT OF INTEREST

On behalf of all authors, the corresponding author declares no conflicts of interest.

OPEN ACCESS

This article is licensed under a Creative Commons Attribution 4.0 International License, which permits use, sharing, adaptation, distribution and reproduction in any medium or format, as long as you give appropriate credit to the original author(s) and the source, provide a link to the Creative Commons licence, and indicate if changes were made. The images or other third party material in this article are included in the article's Creative Commons licence, unless indicated otherwise in a credit line to the material. If material is not included in the article's Creative Commons licence and your intended use is not permitted by statutory regulation or exceeds the permitted use, you will need to obtain permission directly from the copyright holder. To view a copy of this licence, visit http://creativecommons.org/licenses/by/4.0/.

REFERENCES

1. K. Sieradzki and R.C. Newman: *J. Phys. Chem. Solids*, 1987, vol. 48, pp. 1101–13.
2. X. Xie, D. Ning, B. Chen, S. Lu, and J. Sun: *Corros. Sci.*, 2016, vol. 12, pp. 576–84.
3. K. Takamori, S. Suzuki, and K. Kumagai: *Maintenology*, 2004, vol. 3, pp. 52–58.
4. M. Koshiishi, M. Okada, H. Fujimori, and A. Hirano: *Hitachi Rev.*, 2009, vol. 91, pp. 214–17.
5. S. Suzuki, K. Takamori, K. Kumagai, S. Ooki, T. Fukuda, H. Yamashita, and T. Futami: *Pres. Eng. J. Jpn. High Pres. Inst.*, 2004, vol. 42, pp. 188–98.
6. The Kansai Electric Power Co., Inc.: Regarding Significant Indications at Ohi Power Station Unit 3 Pressurizer Spray Line Piping Welds. 2020.
7. N. Ishiyama, M. Mayuzumi, Y. Mizutani, and J. Tani: *J. Jpn. Inst. Mater.*, 2005, vol. 69, pp. 1049–52.
8. O. Raquet, E. Herms, F. Vaillant, and T. Couvant: *Adv. Mat. Sci.*, 2007, vol. 7, pp. 33–46.
9. T. Masuoka, M. Mayuzumi, T. Arai, and J. Tani: *Zairyo-to-Kankyo*, 2007, vol. 56, pp. 93–98.
10. M. Aoki, T. Terachi, T. Yamada, and K. Arioka: *INSS J.*, 2012, vol. 19, pp. 118–30.
11. R. Ihara, T. Hashimoto, and M. Mochizuki: *J. Soc. Mat. Sci. Japan*, 2012, vol. 61, pp. 961–66.
12. L. Yu, K. Nishimoto, and K. Saida: *J. Mat. Sci. Eng. A*, 2023, vol. 13, pp. 13–25.
13. K. Kako, J. Ohta, and M. Mayuzumi: *J. Jap. Inst. Metals*, 2006, vol. 70, pp. 694–99.
14. Y.C. Jean: *Microchem. J.*, 1990, vol. 42, pp. 72–102.
15. O. Shpotyuk, A. Ingram, and Ya. Shpotyuk: *Nucl. Instrum. Methods Phys. Res., Sect. B*, 2018, vol. 416, pp. 102–109.
16. B. Li, V. Krsjak, J. Degmova, Z. Wang, T. Shen, H. Li, S. Sojak, V. Slugen, and A. Kawasuso: *J. Nucl. Mater.*, 2020, vol. 535, pp. 152–80.
17. K. Saarinen, P. Hautojärvi, and C. Corbe: *Semicond. Semimet*, 1998, vol. 51, pp. 209–85.
18. P. Kirkegaard, M. Eldrup, O.E. Mogensen, and N.J. Pedersen: *Comput. Phys. Commun.*, 1981, vol. 23, pp. 307–35.
19. P. Kirkegaard and M. Eldrup: *Comput. Phys. Commun.*, 1974, vol. 7, pp. 401–409.
20. D. Deng, H. Murakawa, and M. Shibahara: *Comp. Mat. Sci.*, 2010, vol. 48, pp. 187–94.
21. J. Park, G. An, N. Ma, and S. Kim: *J. Manuf. Process.*, 2023, vol. 102, pp. 182–94.
22. D. Deng and S. Kiyoshima: *Nucl. Eng. Des.*, 2010, vol. 240, pp. 688–96.
23. T. Kuwabara: *J. Jap. Inst. Light Met.*, 2007, vol. 57, pp. 218–25.
24. P.L. Andresen: *Corrosion*, 2013, vol. 9, pp. 1024–38.
25. S. Suzuki, K. Takamori, K. Kumagai, A. Sakashita, N. Yamashita, C. Shitara, and Y. Okamura: *E.-J. Adv. Maint.*, 2019, vol. 1, pp. 1–29.
26. T. Masumura, Y. Seto, T. Tsuchiyama, and K. Kimura: *Mater. Trans.*, 2019, vol. 59, pp. 222–29.
27. T. Kato, S. Sato, Y. Saito, H. Todoroki, and S. Suzuki: *Adv. X-ray. Chem. Anal. Jpn.*, 2016, vol. 47, pp. 167–72.
28. K. Sawada, K. Maruyama, R. Komine, and Y. Naga: *Tetsu-to-Hagane*, 1997, vol. 83, pp. 54–59.
29. M. Kumagai, K. Akita, M. Imafuku, and S. Ohya: *Mater. Sci. Eng. A*, 2014, vol. 608, pp. 21–24.
30. W. Li, M. Vittorietti, G. Jongbloed, and J. Sietsma: *J. Mater. Sci. Technol.*, 2020, vol. 45, pp. 35–43.
31. L. Yu, K. Saida, H. Araki, K. Sugita, M. Mizuno, K. Nishimoto, and N. Chigusa: *Mater. Sci. Eng. A*, 2020, vol. 796, 140221.
32. W.A. Johnson and K.F. Mehl: *Trans. Am. Inst. Min. (Metall.) Eng.*, 1939, vol. 135, pp. 416–42.
33. M. Avrami: *J. Chem. Phys.*, 1939, vol. 7, pp. 1103–12.
34. M. Fanfoni and M. Tomellini: *IL NUOVO CIMENTO*, 1998, vol. 20D, pp. 1171–82.
35. L. Yu, K. Saida, K. Nishimoto, I. Asai, and N. Chigusa: *Maintenology*, 2022, vol. 20, pp. 83–90.
36. R.V. Patil and B.D. Sharma: *Met. Sci.*, 1982, vol. 16, pp. 389–92.
37. A.F. Smith: *Met. Sci.*, 1975, vol. 9, pp. 375–78.
38. T. Kunitake: *J. Jpn. Inst. Met.*, 1964, vol. 3, pp. 466–76.

Publisher's Note Springer Nature remains neutral with regard to jurisdictional claims in published maps and institutional affiliations.